Supplementary Information (SI) for Energy & Environmental Science.

Designing multi-tentacle electrolytes to enable fast and deep cycling of aqueous Zn batteries at low temperatures

Huimin Wang,‡[a] Mingzi Sun,‡[ab] Yongqiang Yang,[a] Junhua Zhou,[a] Lingtao Fang,[c] Qiyao Huang,[cd], Bolong Huang,*[ab], Zijian Zheng,*[acdefg]

[a] *Department of Applied Biology and Chemical Technology, The Hong Kong Polytechnic University, Hong Kong SAR, China*

[b] *Department of Chemistry, City University of Hong Kong, Hong Kong SAR, China*

[c] *School of Fashion and Textile, The Hong Kong Polytechnic University, Hong Kong SAR, China*

[d] *Research Institute for Intelligent Wearable Systems (RI-IWEAR), The Hong Kong Polytechnic University, Hong Kong SAR, China*

[e] *Research Institute for Smart Energy (RISE), The Hong Kong Polytechnic University, Hong Kong SAR, China*

[f] *The Hong Kong Polytechnic University-Wenzhou Technology and Innovation Research Institute, Wenzhou, Zhejiang Province, China.*

[g] *The Hong Kong Polytechnic University-Daya Bay Technology and Innovation Research Institute, Huizhou, Guangdong Province, China.*

‡ *These authors contributed equally to this work.*

Methods

Electrolyte and electrode preparation

Lithium bis(trifluoromethanesulfonyl)imide (LiTFSI, 99.9%) was purchased from DoDoChem. Zinc trifluoromethanesulfonate ($Zn(OTf)_2$, 98%), zinc perchlorate hexahydrate ($Zn(ClO_4)_2·6H_2O$), zinc chloride ($ZnCl_2$, 99%), zinc sulfate ($ZnSO_4$, anhydrous, 99%), zinc acetate dihydrate ($Zn(Ace)_2·2H_2O$, 99.995%), and lithium sulfate (Li_2SO_4, anhydrous, 99.99%) were purchased from Macklin. Ethylene glycol (EG, analytical reagents, ≥98%), propylene glycol (PG, analytical reagents, ≥98%), glycerol (analytical reagents, ≥98%), N-Methylacetamide (NMA, 99%), succinonitirle (SN, 99%), glyme (≥99.5%), and diglyme (≥99%) were purchased from Aladdin. The electrolytes were prepared by mixing designated salts, organics, and water molecules at a molar ratio of 1.5:4:24 and stirred at room temperature for 1h before use. Before electrochemical testing, a 0.17% (molar fraction) zinc acetate dihydrate ($Zn(Ace)_2·2H_2O$) was incorporated into MTEs to stabilize Zn anode at room temperatures. Due to the minimal amount added, the addition of $Zn(Ace)_2·2H_2O$ does not compromise the freezing point or low-temperature ionic conductivity.

To prepare the $LiMn_2O_4$ (LMO) cathode electrode, LMO active material (Canrd Technology Co. Ltd.), carbon black, and polyvinylidene fluoride were blended in a mass ratio of 8:1:1 in N-methyl-2-pyrrolidine. The obtained slurry was cast on Ti current collector (Carnd Technology Co. Ltd.) and then dried at 85 °C. The mass loading of LMO is 4 ± 0.5 mg cm^{-2} for normal test. For LMO electrodes with high mass loading (~18 mg cm^{-2}), LMO slurry was cast on carbon felt (1mm, thickness) and then dried at 60 °C overnight. The as-obtained LMO mass loading was 18 ± 1 mg cm^{-2}. $NaV_3O_8·1.5H_2O$ (NVO) powder was prepared according to a previous report[1]. The as-prepared NVO powder, carbon-based conductive materials, and polytetrafluoroethylene were mixed at a mass ratio of 6:2:2 and get a paste. The paste was rolled on a Ti mesh (100 mesh) with a NVO mass loading of ~17 ± 1 mg cm^{-2}.

Characterization

The ionic conductivity (σ) of electrolytes was measured at 25, 0, −10, −20, −30, −40 °C in Ti||Ti symmetric cells. The electrochemical impedance spectroscopy (EIS) of the Ti||Ti cell was conducted on an EC-Lab electrochemical workstation (Biologic VMP3, France) with an amplitude of 10 mV and frequencies ranging from 1MHz to 0.1 Hz. The ionic conductivity of electrolytes is calculated according to the following equation:

$$\sigma = \frac{L}{SR}$$

where L is the distance between two Ti electrodes, S is the contact area of two Ti electrodes, and R is the intersection of the experimental curve with the real impedance axis. The phase transition of electrolytes from −65 to 20 °C was measured via the differential scanning calorimeter (Mettler Toledo DSC3) at a heating rate of 10 °C min^{-1}. The ^{1}H and ^{17}O NMR spectra of electrolytes were collected via Jeol ECZ500R 500 MHz NMR spectrometer with D_2O as the field-locking solvent. X-ray diffraction (Rigaku Smart Lab 9kW-Advance) of Zn electrodes was conducted with monochromatic Cu Kα radiation, scanning between 5° and 75° at a rate of 10° min^{-1}. The morphological images of electrodes were acquired by scanning electron microscope (Tescan VEGA3).

Electrochemical measurements

Tafel plots were performed in a typical three-electrode system with the EC-Lab electrochemical workstation (Biologic VMP3, France), where Zn foil acted as the working electrodes, graphite rod as the counter electrode and Ag/AgCl as the reference electrode. The Tafel plots were tested with a scan rate of 5 mV s^{-1} with a potential of ± 0.25 V vs. open-circuit potential. The electrochemical tests were conducted in CR 2032 coin-type cells using glass fiber filters as the separator. Zn foils with a thickness of 100 μm were used in cells if not mentioned. Before use, the Zn foil was polished by softback sanding sponges (3M, USA) and then wiped with ethanol to remove surface oxides or impurities. The cathodes and Zn anodes were punched into disk-shaped electrodes with a diameter of 12 mm for the coin cell assembly. The size of LMO and NVO electrodes used in pouch cells was 3×4 cm^2. Charge/discharge tests of coin and pouch cells were performed on Neware battery test system. Zn||LMO full cells were cycled with a voltage range of 1.5–2.15 V (vs. Zn^{2+}/Zn) at low temperatures. Zn||NVO full cells were examined with a voltage range of 0.2–1.6 V (vs. Zn^{2+}/Zn). For low-temperature testing, all cells were sat at open circuit voltage (OCV) for 5 h before cycling to reach an equilibrium of temperature. For the discharge galvanostatic intermittent titration technique (GITT) test, Zn||LMO cells were discharged at 0.1 C with a pulse time of 10 min, followed by a 1h relaxation. The diffusion coefficients D^{GITT} were determined via the following equation

$$D^{GITT} = \frac{4L^2}{\tau\pi}\left(\frac{\Delta E_s}{\Delta E_t}\right)^2$$

where τ denotes the constant current pulse time, L is the diffusion length of charge carrier in electrodes, equal to the thickness of electrodes, ΔE_s the change of the steady-state voltage during a single-step GITT experiment, and ΔE_t the total change of cell voltage during a constant current pulse τ of a single-step GITT experiment neglecting the IR-drop.

Computational methods

For the study of the freezing behavior of electrolytes with a formula 1.5x:4y:24H_2O, we have carried out theoretical explorations based on density functional theory (DFT) calculations and molecular dynamics (MD) simulations. The MD simulations are performed by using the Forcite method. To investigate the influences of the electrolyte component on the frozen point, we have constructed models consisting of Zn salts (BF_4^-, Cl^-, SO_4^{2-}, ClO_4^-, OTF^-, $TFSI^-$), organic components (EG, PG, glycerol, SN), and water in a ratio of 1.5: 4: 24. The simulations start with geometry optimizations first in 298K to reach the equilibrium state. Then, the MD simulations in the NPT ensemble will be carried out under 1 atm and 298 K and 250 K for 25 ps with a timestep of 1.0 fs, where the COMPASS forcefield has been applied. DFT calculations are performed by the CASTEP package to obtain binding energies and interaction energies of different electrolytes[2]. The generalized gradient approximation (GGA) and Perdew-Burke-Ernzerhof (PBE) functionals are selected to deal with the exchange-correlation interactions[3-5]. The ultrasoft pseudopotentials with ultrafine quality have been selected and the plane-wave cutoff energy has been set to 380 eV. The Broyden-Fletcher-Goldfarb-Shannon algorithm is applied for energy minimization processes and the k-point quality has been set to coarse[6]. For all the geometry optimizations, we have set the following criteria: 1) Hellmann-Feynman forces should be smaller than 0.001 eV/Å; 2) total energy difference should not exceed 5×10^{-5} eV/atom; and 3) maximum displacement should be smaller than 5×10^{-3} Å for each atom.

For the study of solvation structures in MTE-EG-$Zn(ClO_4)_2$, the partial charge of ClO_4^-, $TFSI^-$, OTF^- and EG molecule was calculated using Gaussian 16 code. The 6-311g(d,p) basis functions were applied. The OPLS-AA force field and auxiliary tools of force field (AuToFF) were used to parametrize all atoms, including the bond parameters, angle parameters and the dihedral angles. The parameters of ClO_4^-, $TFSI^-$ and OTF^- are derived from OPLS-2009IL force field. In the MD simulation, 150 $Zn(ClO_4)_2$, 400 EG and 2400 water molecules were randomly inserted into a cube box with a side length of 8.0 nm. The MD simulation was performed in the GROMACS 2021 software package. The steepest descent method was applied to minimize the initial energy with a force tolerance of 1 kJ/(mol^{-1} nm^{-1}) and a maximum step size of 0.002 ps before MD calculations. Periodic boundary conditions were imposed in three directions. The Leapfrog algorithm was used to integrate the Newtonian equation of motion. The MD simulation was processed in an NPT ensemble and the simulation time was 20 ns. In NPT simulations, the pressure was maintained at 1 bar by the

Berendsen barostat in an isotropic manner; and the temperature was maintained by the V-rescale thermostat at 298.15 K. A cutoff of 1.0 nm was employed to calculate the short-range van der Waals interactions and electrostatic interactions.

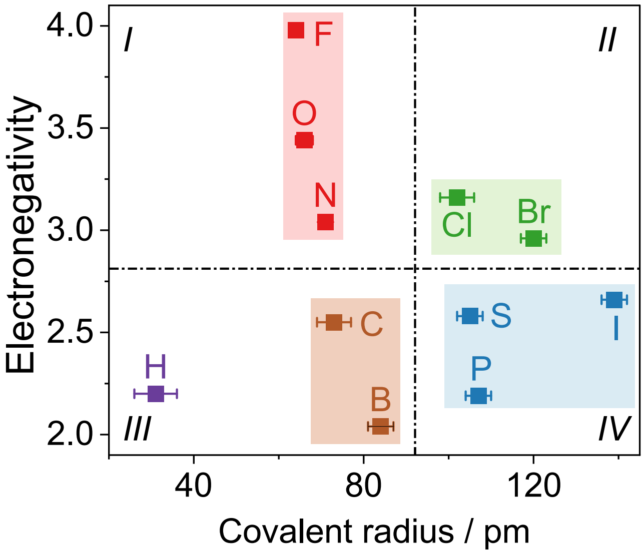

Supplementary Figure 1. Comparison of the electronegativity of elements and their corresponding covalent radii.

Discussion of Supplementary Figure 1:

Effective H-bonds with H atoms in water require H-bond-acceptor atoms to be similar in size to H and possess strong electronegativity for optimal orbital overlap. As shown in Supplementary Figure 1, F, O, and N atoms in region I demonstrate a high tendency for H-bonding due to their electronegativity and suitable covalent radii, while atoms in regions II, III, and IV have lower electronegativity or larger covalent radii and are less effective.

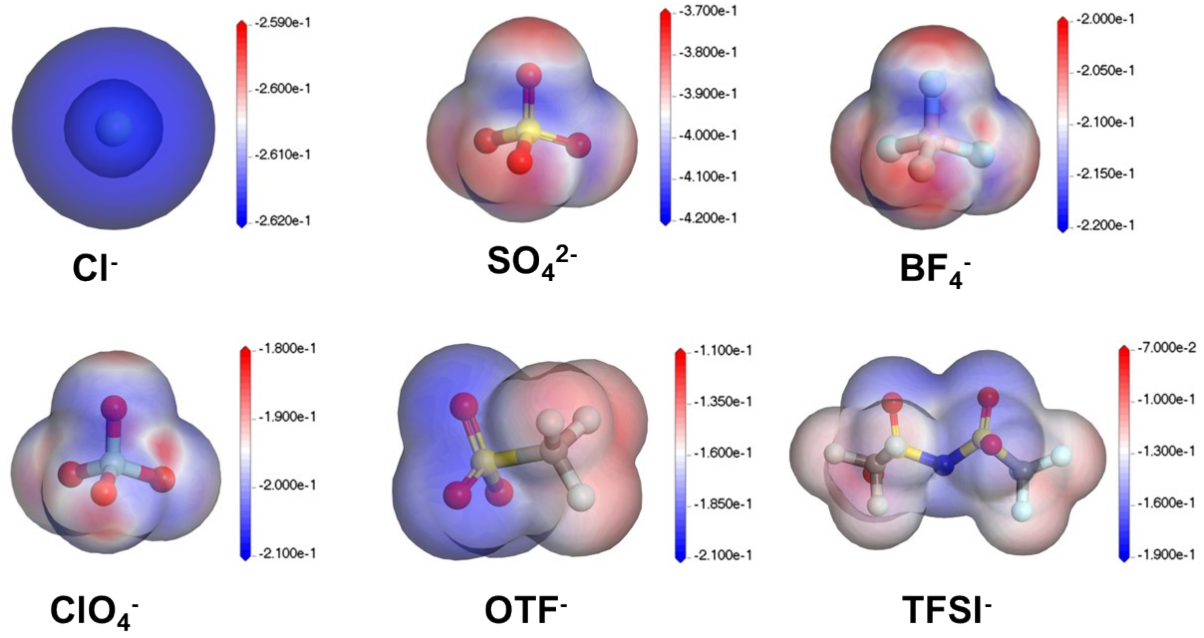

Supplementary Figure 2. ESP mapping of anions. Isovalue is set to 0.17, and the color bar is in Hartree units.

Discussion of Supplementary Figure 2

We have compared a series of different anions with distinct electrostatic potential (ESP), which results in the varying preference to interact with water molecules. For Cl^-, the ESP distributions are uniform while other anions all show evident contrast in the ESP mapping. For BF_4^-, SO_4^{2-}, and ClO_4^-, it is noted that the most negative ESP values are all located near the O sites, which play as the main sites to interact with H atoms from water molecules. For OTF^- and $TFSI^-$, the O and N sites still exhibit the most negative ESP values while the corresponding ESP values of F sites are much weaker.

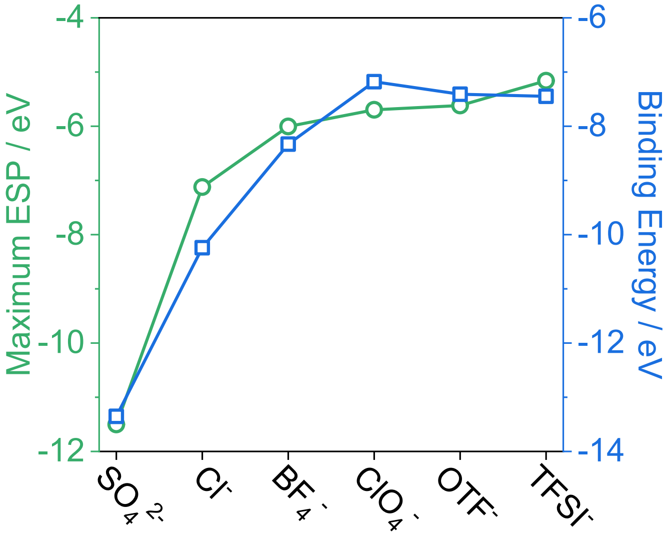

Supplementary Figure 3. Correlation between the most negative electrostatic potential (ESP) values and the binding energies of Zn^{2+} with various anions.

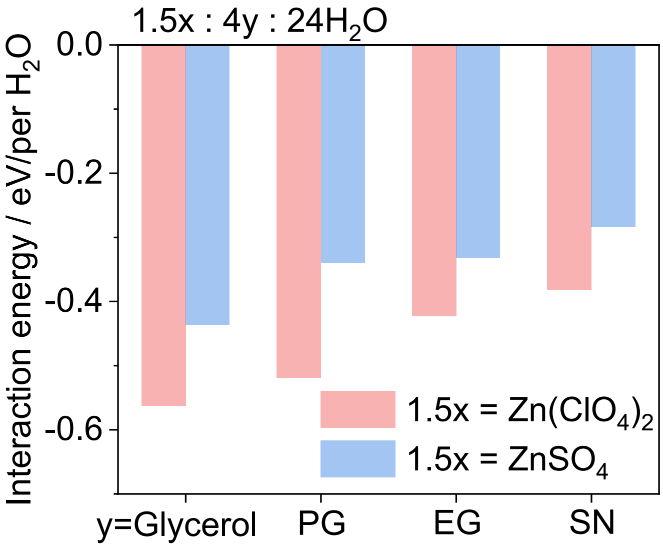

Supplementary Figure 4. Overall interaction energies in electrolytes with the formula 1.5x:4y:24H_2O.

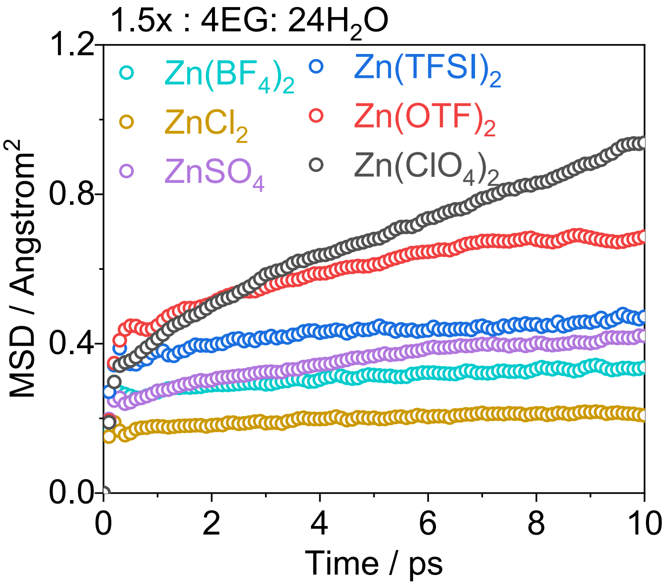

Supplementary Figure 5. Mean square displacement (MSD) values for electrolytes with the composition of 1.5x:4EG:24H_2O. Salts (x) were varying from $ZnCl_2$, $Zn(BF_4)_2$, $ZnSO_4$, $Zn(TFSI)_2$, $Zn(OTf)_2$, $Zn(ClO_4)_2$.

Discussion of Supplementary Figure 4, 5

The investigation of intermolecular interactions and ion migration in electrolytes also demonstrates lower freezing tendency in electrolytes with multi-tentacle salts and organics. Analysis of overall interaction energies in electrolytes with the formula 1.5x:4y:24H_2O (Supplementary Figure 4) shows that those with x = $Zn(ClO_4)_2$ have more negative interaction energies than those with x = $ZnSO_4$ across various y (EG, PG, glycerol, and SN). Furthermore, electrolytes containing EG, PG, or glycerol exhibit stronger interactions than those with SN when varying x between $Zn(ClO_4)_2$ and $ZnSO_4$. These enhanced interactions prevent the orderly rearrangement of a large proportion of water molecules at low temperatures. We also assessed the mean square displacement (MSD) of different electrolytes with the formula 1.5x:4EG:24H_2O to investigate ion migration at 250 K (Supplementary Figure 5). The MSD values for ions follow this order: $ZnCl_2 < Zn(BF_4)_2 < ZnSO_4 < Zn(TFSI)_2 < Zn(OTf)_2 < Zn(ClO_4)_2$, indicating that electrolytes with $Zn(OTf)_2$, $Zn(ClO_4)_2$, and $Zn(TFSI)_2$ have lower freezing tendencies than those with $ZnCl_2$, $Zn(BF_4)_2$, and $ZnSO_4$.

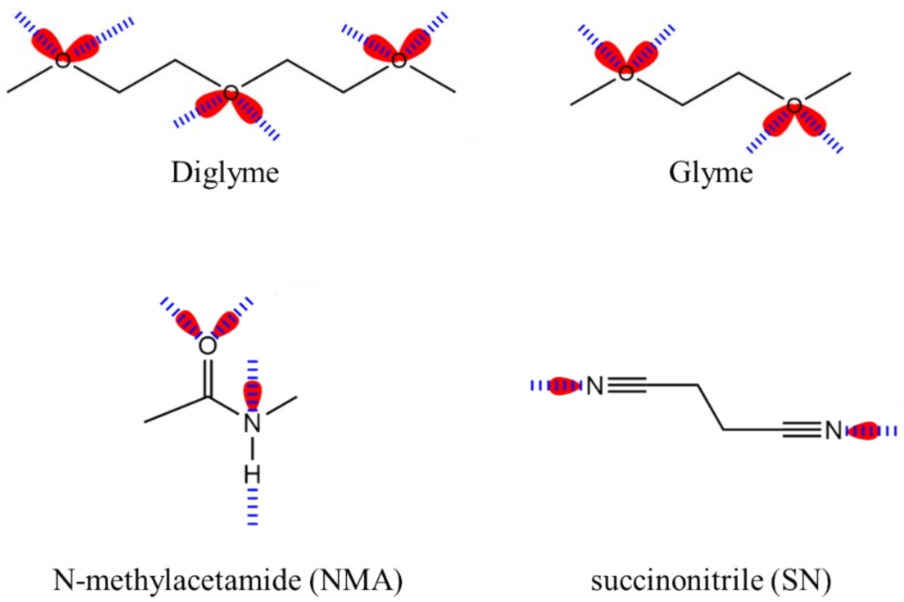

Diglyme

Glyme

N-methylacetamide (NMA)

succinonitrile (SN)

Supplementary Figure 6. Potential H-bonding sites on dilyme, glyme, N-methylacetamide (NMA) and SN. Red ellipses indicate electron lone pairs that can act as H-bond acceptors. The H atom in the -NH group of organics can serve as an H-bond donor. Blue dashed lines represent possible H-bonds.

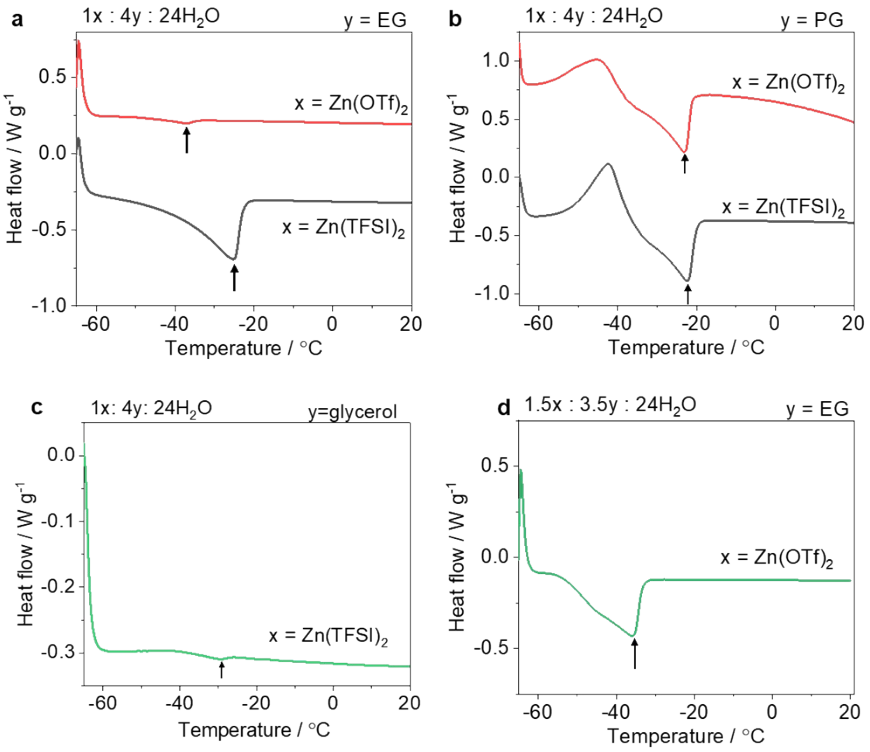

Supplementary Figure 7. DSC curves of electrolytes with the formula 1x:4y:24H_2O (**a**–**c**) and the electrolyte with the formula 1.5x:3.5y:24H_2O (**d**) during heating from −65 to 20 °C.

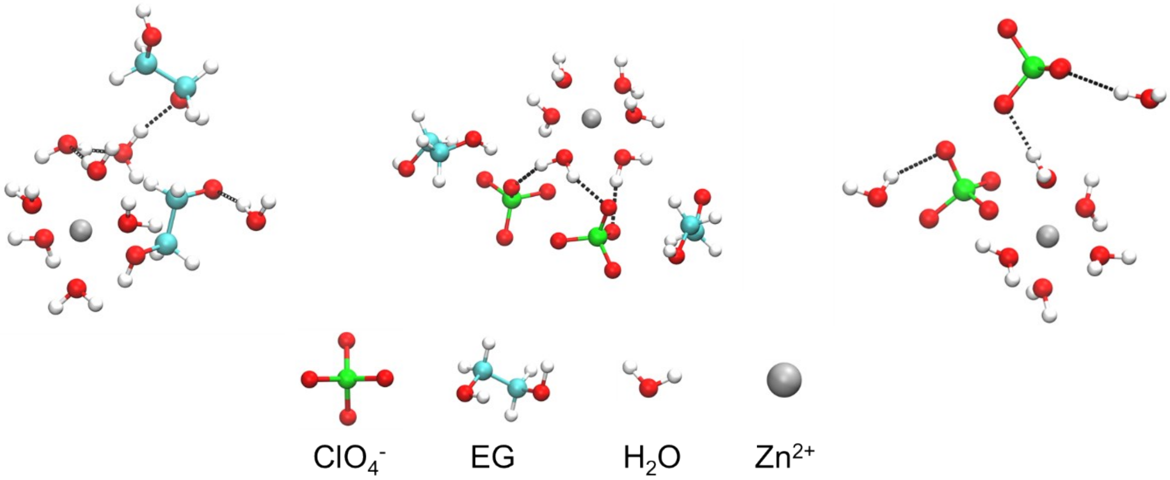

Supplementary Figure 8. Representative solvation structures in MTE-EG-Zn(ClO_4)$_2$. Water molecules in MTE-EG-Zn(ClO_4)$_2$ are well confined through coordination and H-bond effects. The black dashed line represents the H-bonds between multi-tentacle organics-H_2O and multi-tentacle anions-H_2O.

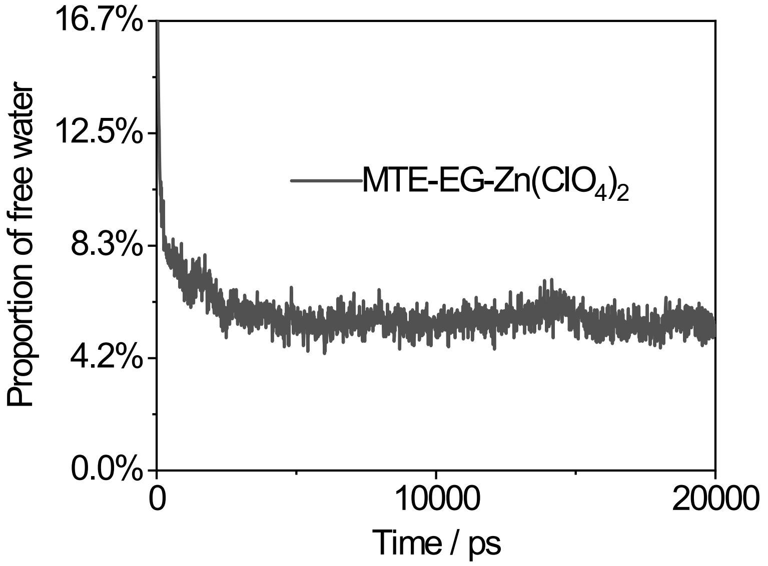

Supplementary Figure 9. The analysis of free water molecules in MTE-EG-Zn(ClO_4)$_2$. Free water molecules are those not involved in coordination or H-bonding with anions and organics.

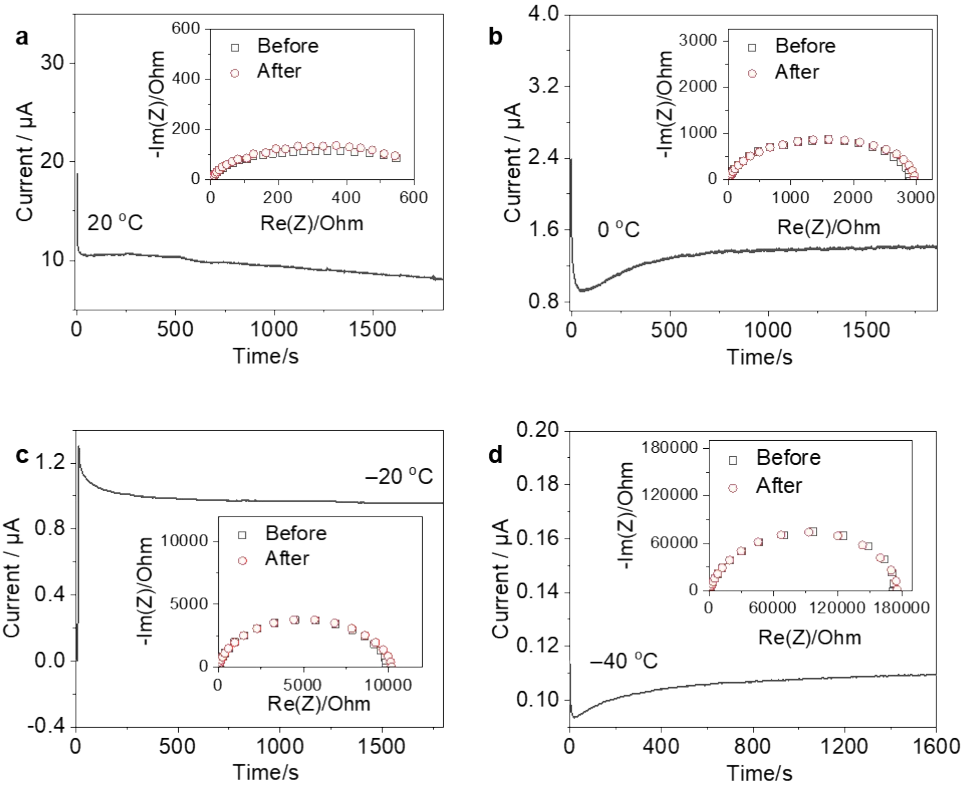

Supplementary Figure 10. The steady-state polarization curves of MTE-EG-Zn$(ClO_4)_2$ at a bias voltage of 10 mV at 20 °C (**a**), 0 °C (**b**), −20 °C (**c**), and −40 °C (**d**). The insets display the electrochemical impedance spectra before and after polarization.

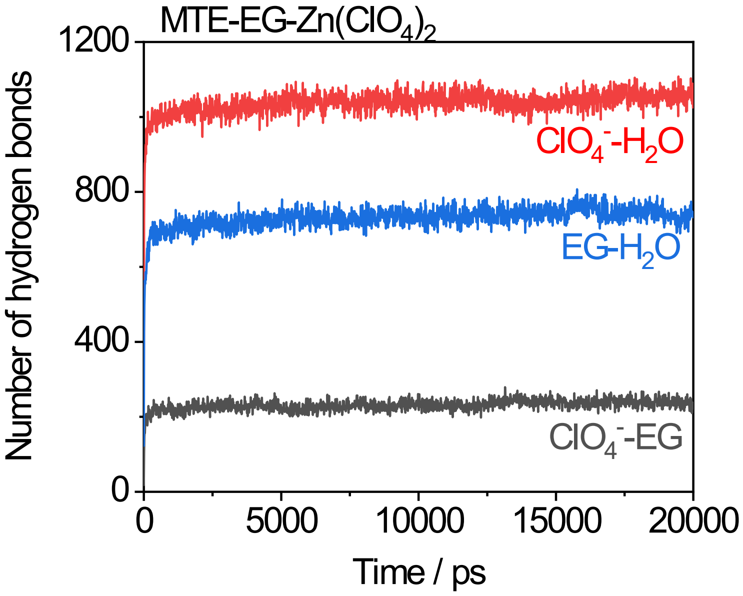

Supplementary Figure 11. The analysis of H-bond numbers originating from EG-H_2O, anions-H_2O, and anions-EG in MTE-EG-$Zn(ClO_4)_2$.

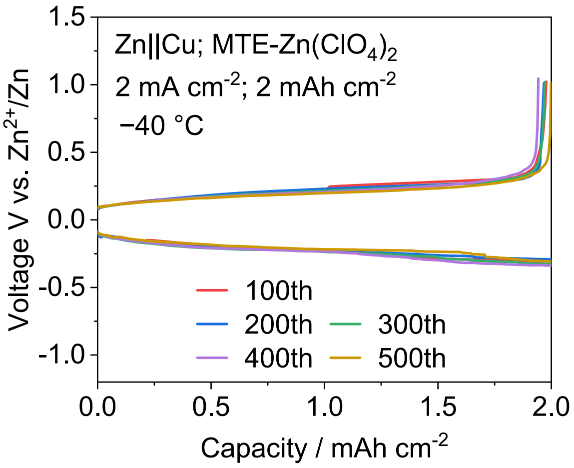

Supplementary Figure 12. Representative voltage profiles of Zn||Cu cells in MTE-EG-$Zn(ClO_4)_2$ at −40 °C and 2 mA cm^{-2} /2 mAh cm^{-2}.

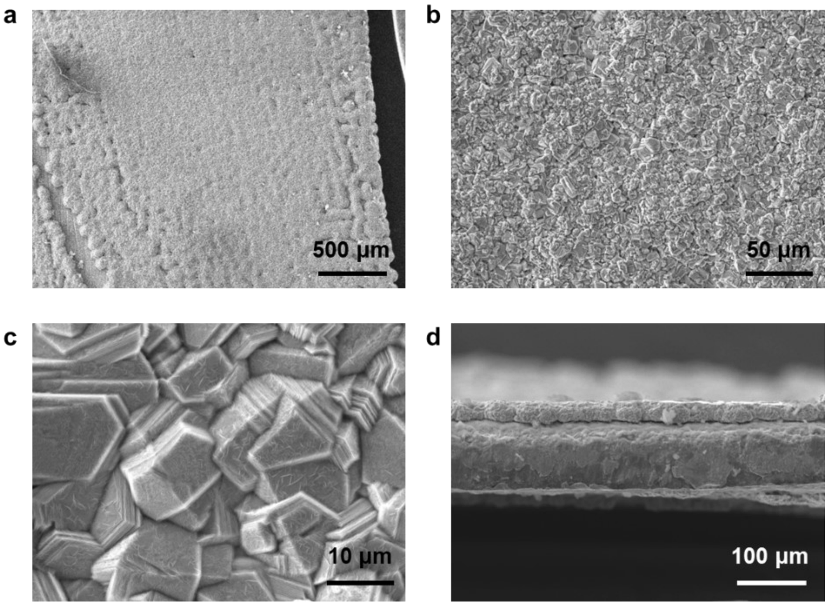

Supplementary Figure 13. The top (**a-c**) and cross-sectional (**d)** SEM images of the Zn deposits on Cu foil after plating at 10 mA cm^{-2} for 1h in MTE-$Zn(ClO_4)_2$.

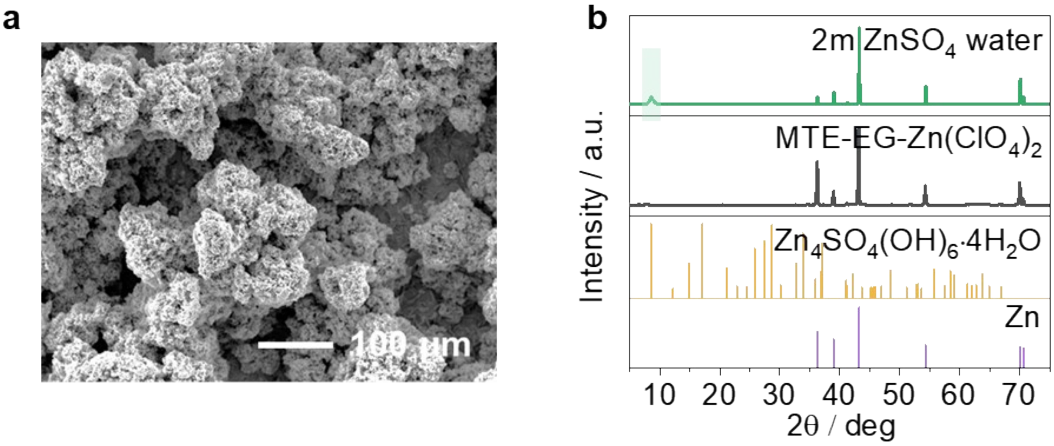

Supplementary Figure 14. (**a**) The morphology of Zn deposition recovered from 2m $ZnSO_4$ in water after plating 1h at 10 mA cm^{-2}. (**b**) XRD patterns of Zn deposition recovered from 2m $ZnSO_4$ in water and MTE-EG-Zn(ClO_4)$_2$. The impurity $Zn_4SO_4(OH)_6{\cdot}4H_2O$ was detected on Zn recovered from the 2m $ZnSO_4$ in water, while only pure Zn was observed in Zn recovered from MTE-EG-Zn(ClO_4)$_2$.

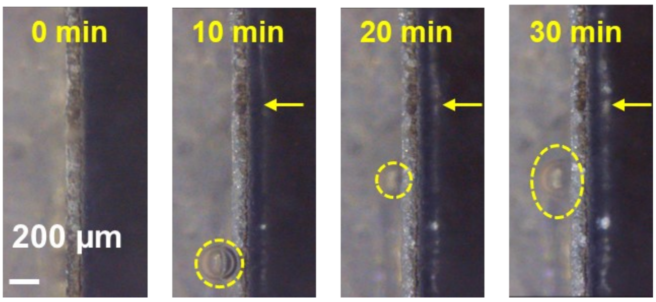

Supplementary Figure 15. In-situ observation of Zn plating in Zn||Zn cells in 2m $ZnSO_4$ at a current density of 10 mA cm^{-2}. Bubbles are highlighted in yellow circles. Arrows indicate the side with Zn deposition.

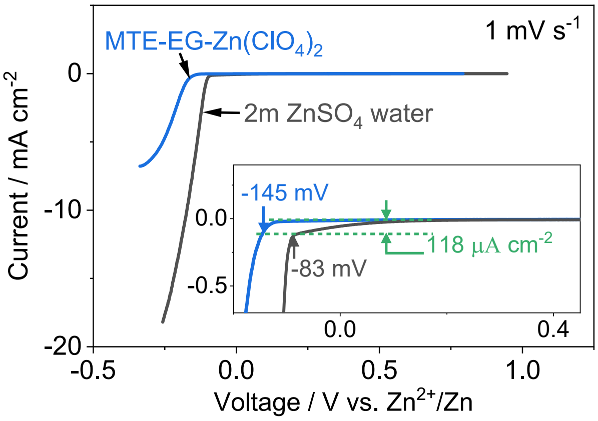

Supplementary Figure 16. Cathodic LSV of MTE-EG-Zn(ClO_4)$_2$ and commonly-used 2m $ZnSO_4$ water obtained on non-active Ti electrode at 1 mV s^{-1}. Inset: magnified view at the cathodic region. The hydrogen evolution current observed at −83 mV versus Zn^{2+}/Zn in sulfate aqueous counterpart was virtually eliminated in MTE-EG-Zn(ClO_4)$_2$.

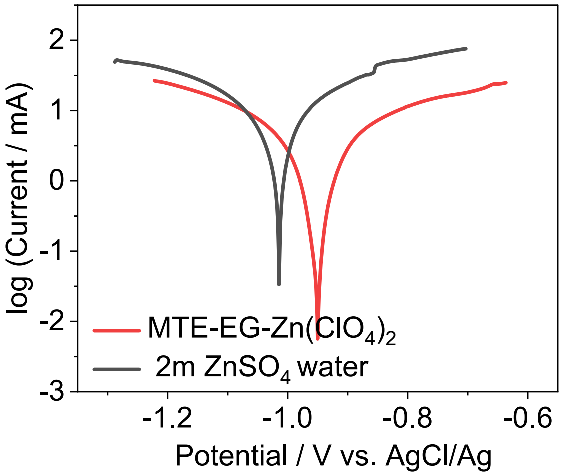

Supplementary Figure 17. The Tafel plots in MTE-EG-Zn$(ClO_4)_2$ and 2m $ZnSO_4$ water examined at a scan rate of 5 mV s^{-1} and a potential of ± 0.25 V vs. open-circuit potential. Tafel plots of Zn in MTE-EG-Zn$(ClO_4)_2$ show a positive shift of potentials and reduced currents achieved, manifesting a lower corrosion rate and suppressed hydrogen evolution reaction (HER).

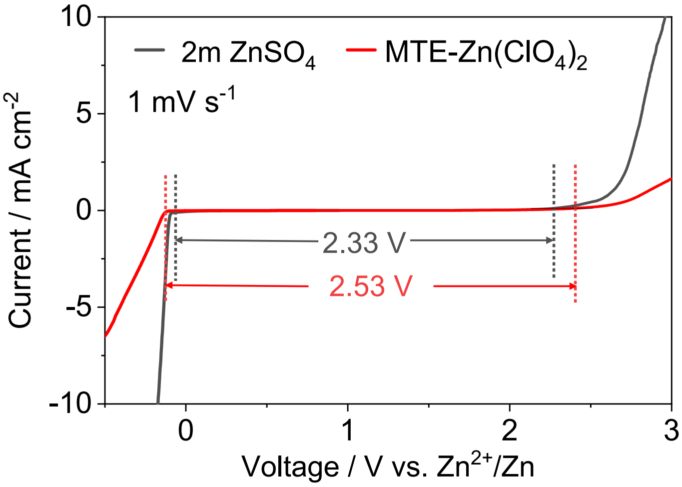

Supplementary Figure 18. Cathodic and anodic LSV curves of MTE-EG-$Zn(ClO_4)_2$ and conventional 2M $ZnSO_4$ aqueous electrolyte. The electrochemical stability windows were determined at a current density threshold of ± 0.1 mA cm^{-2}.

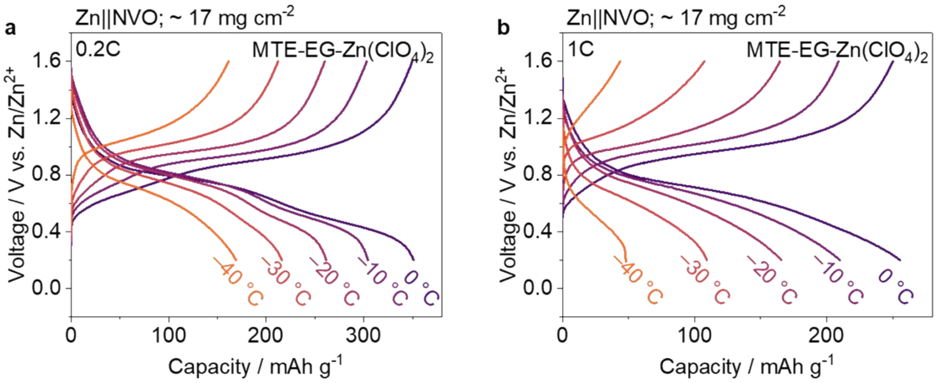

Supplementary Figure 19. Voltage profiles of Zn||NVO (~17 mg cm^{-2}) evaluated at 0.2C (**a**) and 1C (**b**) in MTE-EG-$Zn(ClO_4)_2$ at varying temperatures ranging from 0 to −40 °C.

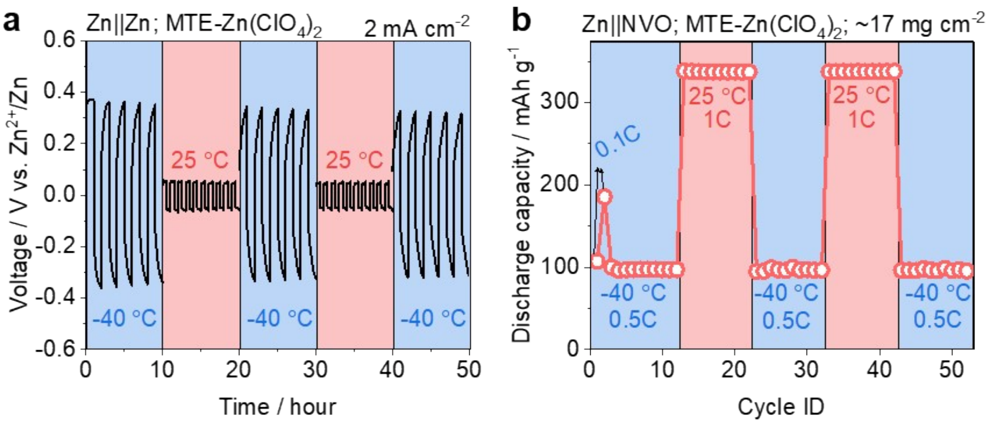

Supplementary Figure 20. Temperature-cycling performance of (**a**) Zn||Zn symmetric cells at 2 mA cm^{-2} and (**b**) Zn||NVO (~17 mg cm^{-2}) full cells at 0.5C (−40 °C) and 1C (25 °C).

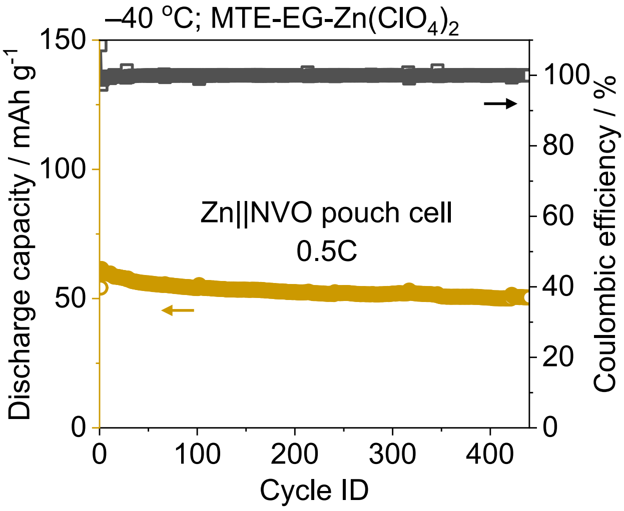

Supplementary Figure 21. Stability of the Zn||NVO pouch cell with MTE-EG-Zn(ClO_4)$_2$ at −40 °C and a current of 0.5C.

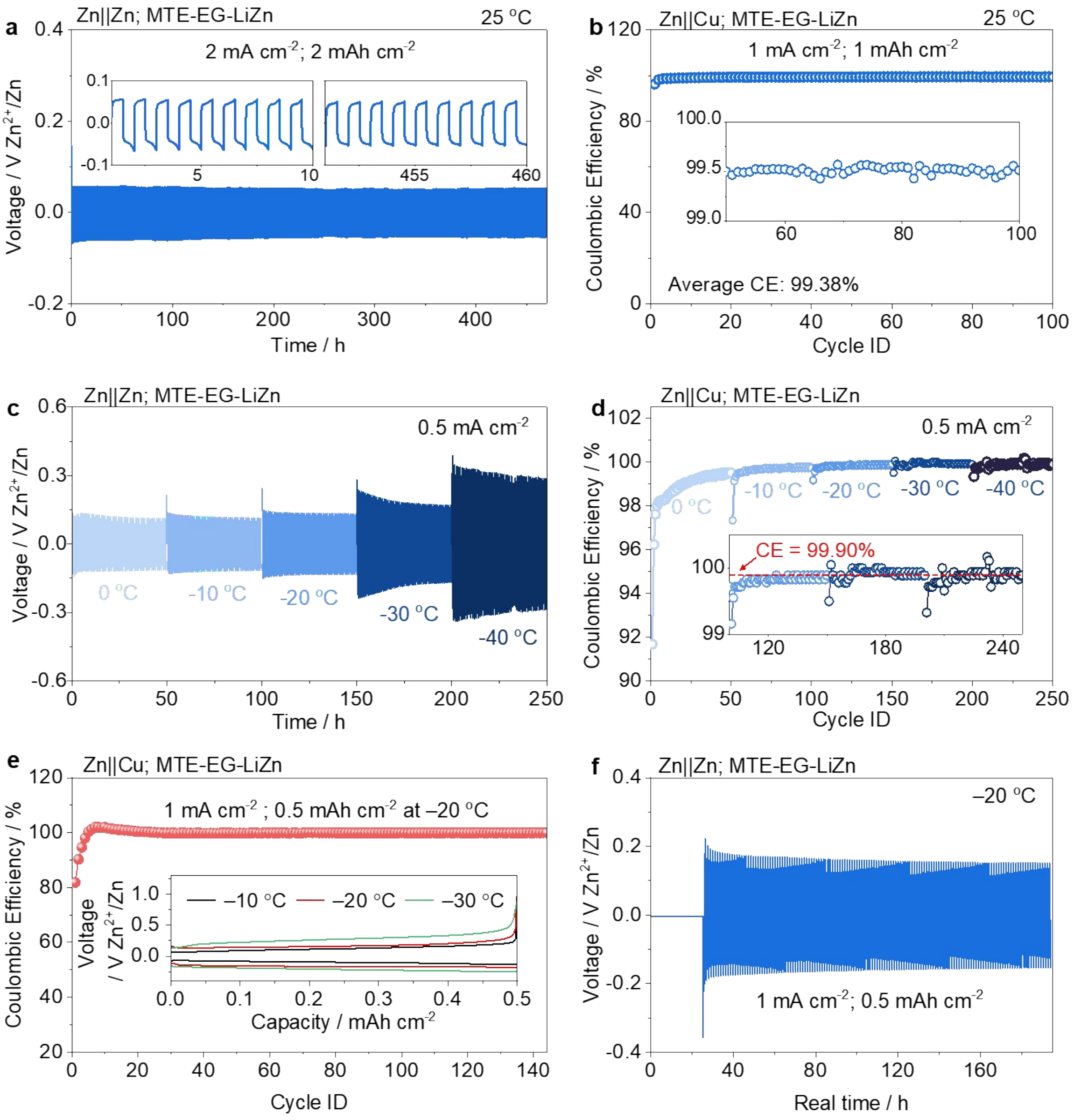

Supplementary Figure 22. (**a**) Voltage profiles of Zn||Zn symmetric cells at 2 mA cm^{-2}/2 mAh cm^{-2} in MTE-EG-LiZn at 25 °C. Insets: magnified view at 0–10 h and 450–460 h. (**b**) Coulombic efficiency of Zn plating/stripping in Zn||Cu asymmetrical cells at 1 mA cm^{-2} /1 mAh cm^{-2} in MTE-EG-LiZn at 25 °C. Insets: magnified view at 50−100 cycles. (**c, d**) Voltage profiles of Zn||Zn symmetric cells (**c**) and reversibility of Zn plating/stripping in Zn||Cu asymmetrical cells (**d**) with MTE-EG-LiZn electrolyte at 0.5 mA cm^{-2}, evaluated at decreasing temperatures from 0 to −40 °C. (**e, f**) Coulombic efficiency of Zn plating/stripping in Zn||Cu asymmetrical cells (**e**) and voltage profiles of Zn plating/stripping in Zn||Zn symmetric cells (**f**) at 1 mA cm^{-2} and 0.5 mAh cm^{-2} in MTE-EG-LiZn at −20 °C. Inset of (**e**): voltage profiles of Zn plating/stripping in Zn||Cu asymmetric cells at a high current density of 1 mA cm^{-2} with decreasing temperatures from −10 to −30 °C.

Discussion of Supplementary Figure 22:

The Zn plating/stripping in MTE-EG-LiZn shows high reversibility and stability across a wide temperature window ranged from 25 to −40 °C. For room temperature testing (Supplementary Figure

22a, b), Zn||Zn symmetric cells sustain for 460 hours at 2 mA cm^{-2}/2 mAh cm^{-2}; an average Coulombic efficiency of 99.38% can be achieved when Zn||Cu cell with MTE-EG-LiZn were cycled at 1 mA cm^{-2}/1 mAh cm^{-2}. For low temperature testing, the overpotential of Zn||Zn cells with MTE-EG-LiZn shows only a modest increase from 165 mV at 0 °C to 482 mV at −40 °C (Supplementary Figure 22c) when cycled at 0.5 mA cm^{-2}, demonstrating the fast Zn^{2+} transport and de-solvation process. As shown in Supplementary Figure 18d, when Zn||Cu cells were evaluated at 0.5 mA cm^{-2}, an initial Coulombic efficiency of 91.67% was achieved and increased to 99.5% after 44 cycles at 0 °C. CE kept increasing to ~99.90% gradually when decreasing temperatures to −20, −30, and −40 ℃, indicating high reversibility of Zn anode. Zn plating/stripping in MTE-EG-LiZn also exhibits high reversibility and stability even at a higher current density of 1 mA cm^{-2} at low temperatures ranging from −10 to −30 ℃ (Supplementary Figure 22e, f).

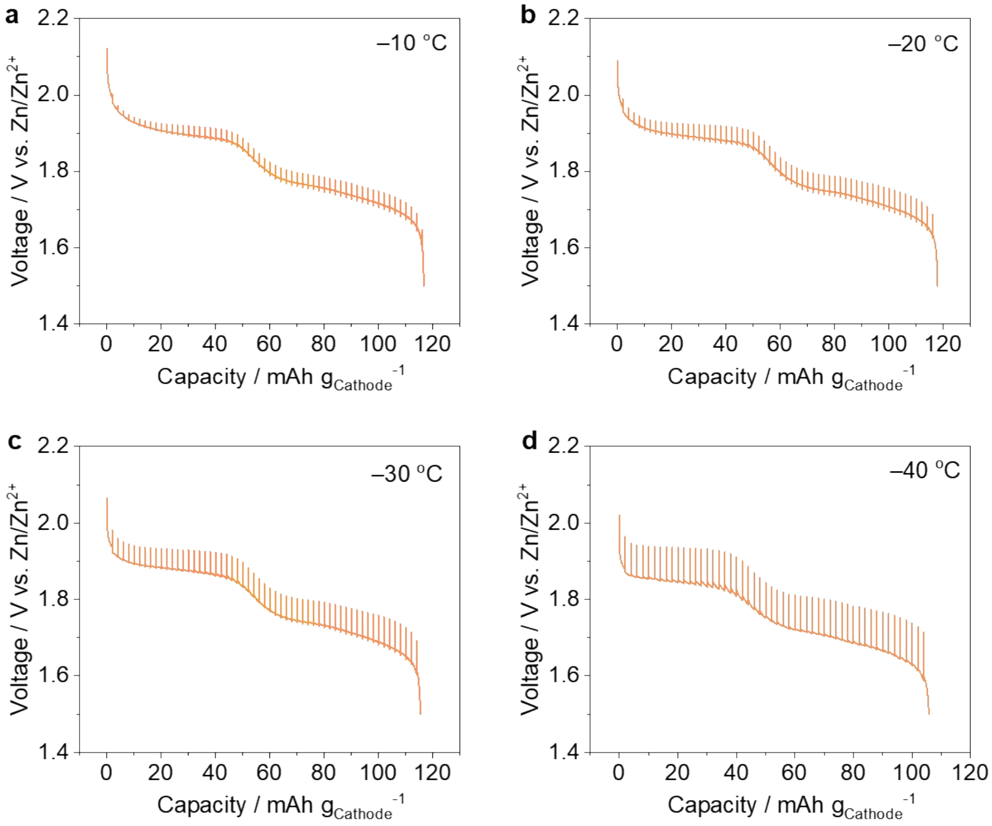

Supplementary Figure 23. The discharge GITT curves of LMO in MTE-EG-LiZn evaluated at (**a**) 0 °C, (**b**) −10 °C, (**c**) −20 °C (**d**) −30 °C and (**e**) −40 °C. The GITT was evaluated at a series of galvanostatic discharge pulses of 10 min at 0.1C followed by 1 h relaxation.

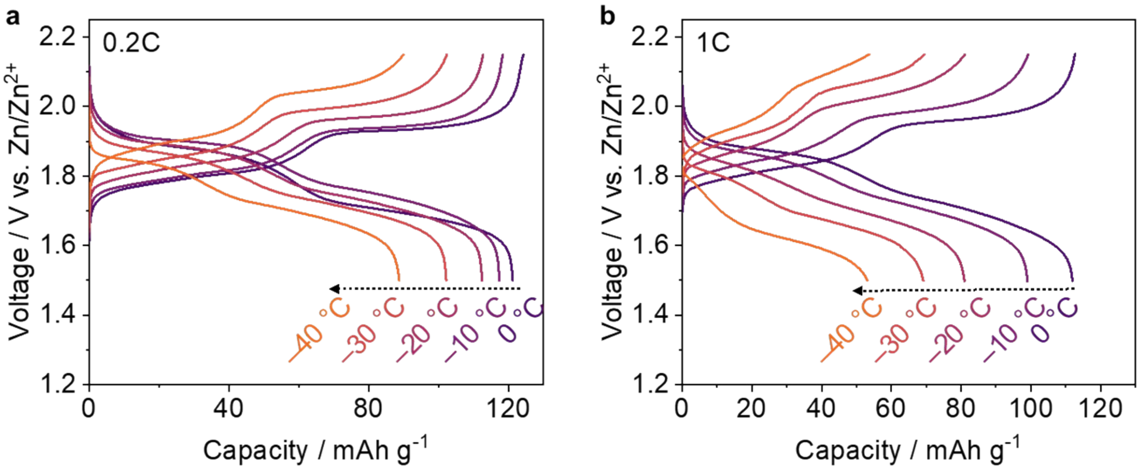

Supplementary Figure 24. Volage profiles of Zn||LMO batteries evaluated at 0, −10, −20, and −30, −40 °C at 0.2C (**a**) and 1C (**b**).

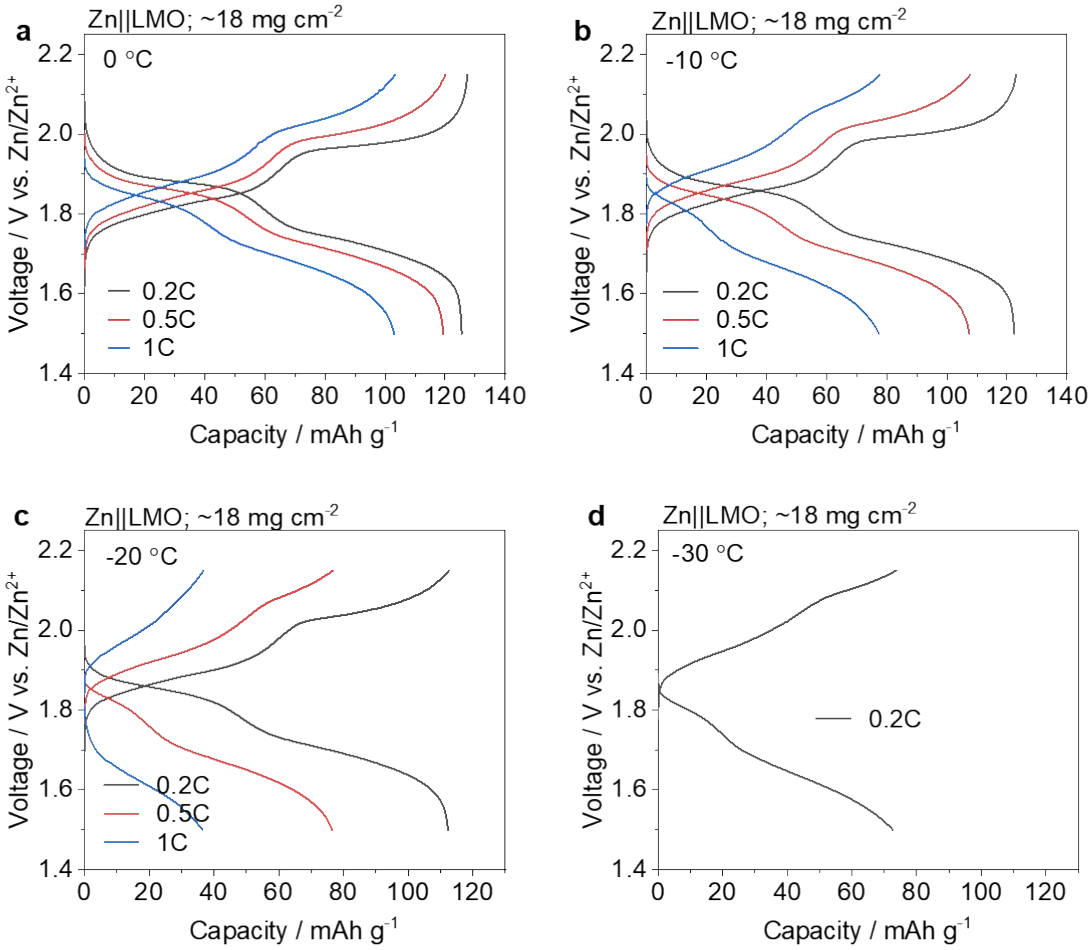

Supplementary Figure 25. Voltage profiles of Zn||LMO cells with a mass loading of ~18 mg cm^{-2} in MTE-EG-LiZn, evaluated at different C rates and low temperatures.

Table S1. Comparison of mass loading, areal capacity, areal current, testing temperature, specific energy between our work and other reported low-temperature Zn batteries. Specific energy was calculated based on the mass of active material at cathodes.

Cathode	**Mass loading**	**Areal capacity**	**Areal current**	**Testing temperature**	**Specific energy (based on cathode)**	**Ref.**
	mg cm^{-2}	**mAh cm^{-2}**	**mA cm^{-2}**	**^{o}C**	**Wh kg^{-1}**	
Poly(2,3-dithiin-1,4-benzoquinone) (PDB)	0.21	0.021	0.00315	25	80.3	Ref.34
				-10	55.7	
				-25	34.2	
V_2O_5	2~3	0.481	~2.5	25	109.74	Ref.14
			~1.25	-15	77.66	
V_2O_5	5	1.600	5	25	241.06	Ref.15
				-20	106.17	
V_2O_5	1.6±1	0.293	0.128	25	139.26	Ref.38
Polyaniline (PANI)	~2	0.321	0.2	25	132.65	Ref.35
				-20	110.4	
				-40	53.8	
V_2O_5	2-3.5	0.488	0.275	20	157.3	Ref.21
				-20	113.5	
Our LMO (normal electrodes)	4±0.5	0.497	0.096	0	216.1	
		0.470		-10	212.6	
		0.450		-20	201.6	
		0.409		-30	181.2	
		0.355		-40	154.4	
	4±0.5	0.448	0.48	0	198.8	
		0.396		-10	174.8	
		0.324		-20	140.5	
		0.277		-30	117.6	
		0.213		-40	87.2	
Our LMO (High loading)	18±1	2.260	0.432	0	225.67	
		2.204		-10	218.03	
		2.021		-20	197.17	
		1.324		-30	121.26	
Our NVO (High loading)	17±1	5.969	1.19	0	236.2	
		5.172		-10	221.3	
		4.447		-20	191.1	
		3.675		-30	153.3	
		2.873		-40	110.4	

References:

1. Y. K. Li, Z. M. Huang, P. K. Kalambate, Y. Zhong, Z. M. Huang, M. L. Xie, Y. Shen and Y. H. Huang, *Nano Energy*, 2019, **60**, 752-759.
2. S. J. Clark, M. D. Segall, C. J. Pickard, P. J. Hasnip, M. J. Probert, K. Refson and M. C. Payne, *Z Kristallogr*, 2005, **220**, 567-570.
3. J. P. Perdew, K. Burke and M. Ernzerhof, *Phys Rev Lett*, 1996, **77**, 3865-3868.
4. P. J. Hasnip and C. J. Pickard, *Comput Phys Commun*, 2006, **174**, 24-29.
5. J. P. Perdew, J. A. Chevary, S. H. Vosko, K. A. Jackson, M. R. Pederson, D. J. Singh and C. Fiolhais, *Physical Review B*, 1992, **46**, 6671-6687.
6. J. D. Head and M. C. Zerner, *Chemical Physics Letters*, 1985, **122**, 264-270.